# Nancy Grace Roman Space Telescope (Roman)
# Technical Report

| | |
|---|---|
| Title: The Background Spectra for the Roman/WFI Exposure Time Calculator | Doc #: Roman-STScI-000481, SC-01<br>Date: January 31, 2023<br>Rev: - |
| Authors: R.E. Ryan Jr. and J. MacKenty Phone: 410-338-4352 | Release Date: March 27, 2023 |


## ABSTRACT

We report on the current state (after August 2020) of the spectral components in the exposure-time calculator, Pandeia, for the Wide-Field Instrument on the Nancy Grace Roman Space Telescope. The Zodiacal, Galactic, and extragalactic backgrounds are taken from the catalog of backgrounds compiled for the James Webb Space Telescope, for a suite of different assump-tions. In this report, we present a new calculation for the total thermal background based on engineering data provided by the Goddard Space Flight Center. These data describe the temperature, emissivity, and solid angle for each physical component of the telescope and/or optics. Therefore, the composite spectrum is effectively a weighted sum of blackbody spectra, and is reported in Fν -based units of MJy/sr. This spectrum supplants the former thermal background model that was taken from the James Webb Space Telescope. We recommend this work be revisited as new engineering data and/or observations become available.


## 1 Introduction

The exposure-time calculator (ETC) is a key component used by the observing community in preparing and understanding observations. One critical input to an ETC is the spectral properties of the background, whose inclusion generally decreases the signal-to-noise ratio. The current background models for the Wide-Field Instrument (WFI) on the Nancy Grace Roman Space Telescope (Roman) are adapted from those for the James Webb Space Telescope (JWST). However, one of the new results of this work will be a new model for the thermal background: the radiation incident on the detector that arises from the physical components within the telescope or instrument. Although the foremost role of this work is to improve the ETC, the resultant spectrum may be useful to other analyses, so it can be found in the Pandeia engine (Pontoppidan et al. 2016).

This report is organized as follows: Section 2 recounts the current state of the astrophysical background sources, Section 3 presents our determination of the thermal background spectrum, and Section 4 concludes with work for the future.

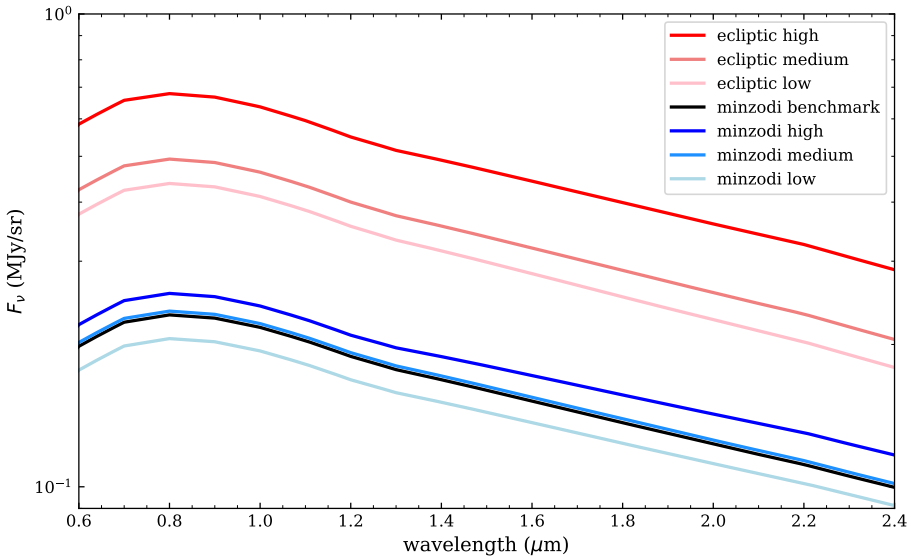


Figure 1: Existing infield (generally unresolved astrophysical sources in the field, not directly related to properties of the detector or telescope) background spectra. These spectra are taken directly from the model of JWST backgrounds, but are only considered for a finite set of observations (ie. ecliptic vs. minzodi), as described in § 2.

## 2 Existing Astrophysical Backgrounds

The existing astrophysical backgrounds are taken from the JWST model, which includes contributions from Zodiacal, Galactic, and extragalactic sources. Since some of these components depend on the telescope attitude and/or observation date (Zodiacal and Galactic), the JWST model permits pointing and date keywords. However, the current Roman ETC is much simpler, and instead only gives users a choice between a minimum Zodiacal (hereafter, minzodi) and on-ecliptic (hereafter, ecliptic) pointing, which are given in Galactic $(\ell, b)$ and ecliptic coordinates $(\lambda, \beta)$:

$$\begin{aligned} \text{minzodi} &= \begin{cases} (\ell, b) = (319.^\circ 486, -20.^\circ 1642) \\ (\lambda, \beta) = (266.^\circ 3, -50^\circ) \end{cases} \\ \text{ecliptic} &= \begin{cases} (\ell, b) = (276.^\circ 335, 60.^\circ 1885) \\ (\lambda, \beta) = (180^\circ, 0^\circ). \end{cases} \end{aligned} \tag{1}$$

Additionally, one can scale these backgrounds with three prescribed levels (low, medium, and high). Finally, there is a "benchmark" model that represents the typical high Galactic pointing for blank field observations. We show this collection of models in Figure 1.

## 3 Determination of Thermal Spectrum

The data described below was delivered by David Hughes at Goddard Space Flight Center (GSFC; approximately summer 2020), and included temperature, emissivity, and effective

solid angle for each physical component that may project light onto the detector. The data are tabulated in an Excel spreadsheet: `HLS_F184_20200629.xlsx`. We present the full list of physical components and a brief description of each in Table 1.

Table 1: Physical Components

| Component | Sub-Component | Description |
|---|---|---|
| Instrumental | aperture | knife-edge ring between the filter and detectors |
| | bezels | retaining ring around the filter |
| | COBA_MLI | multi-layer insulation inside the COBA |
| | COBA | Cold-Optical Baffle Assembly (tube between the filters and detectors) |
| | FPA | the focal plane filter |
| | filter | the filter element |
| | frame | aluminum structure in the instrument |
| | heater | heaters on the filter-wheel housing |
| | wheel | the filter wheel |
| Baffle | cassegrain | baffle mounted on the central hoel of the primary |
| | PM_aperture | the primary mirror aperture |
| | pupil | the pupile mask mounted on the telescope side of the filter |
| Optics | F1 | first fold mirror behind the primary |
| | F2 | second fold mirror |
| | PM | the primary mirror |
| | SM | the secondary mirror |
| | TM | the tertiary mirror |
| Structure | AOM | aft-optics module (box that holds the fold and tertiary mirrors) |
| | DAC | deployable aperture cover |
| | OBA | outer-barrel assembly (main light shield for the telescope) |
| | PM_mount | the primary mirror mount |
| | SMSTs | secondary-mirror support tubes |
| | SM_housing | the secondary mirror housing |

Table 2: Adopted Properties of Roman and/or WFI

| Property | Value |
|---|---|
| pixel scale | $0\farcs11$ |
| | 10 $\mu$m |
| primary mirror collecting area | 4.38562 $m^2$ |

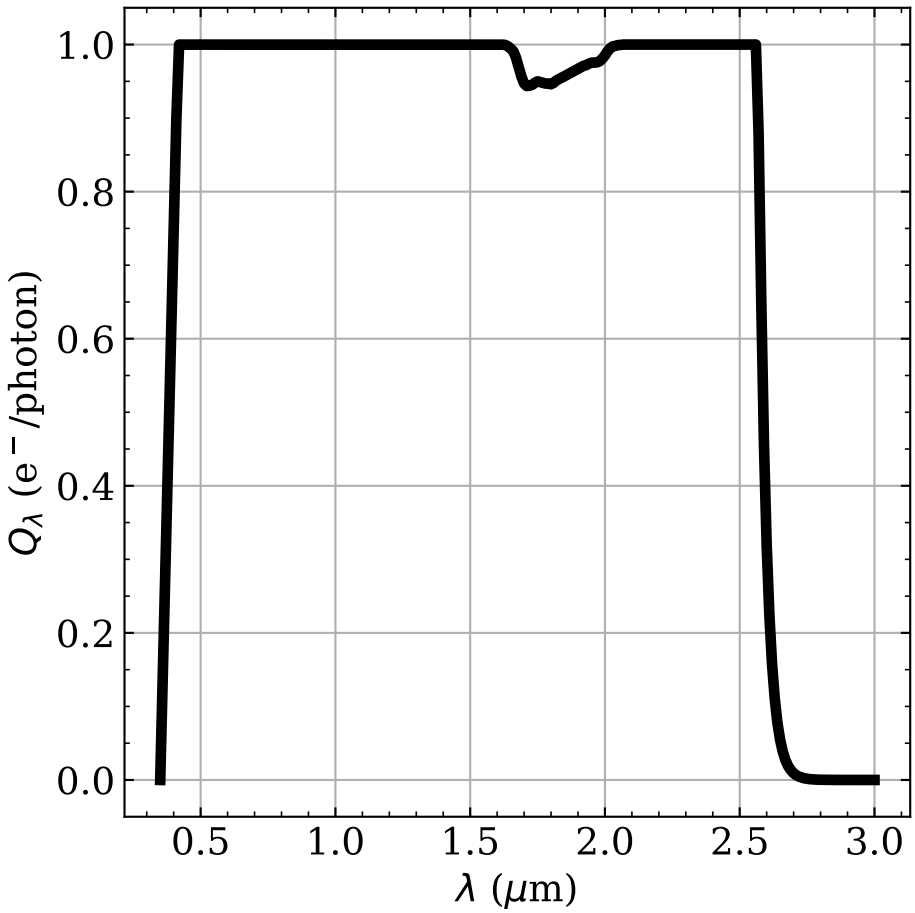


Figure 2: Quantum efficiency. The conversion between incident photons and the number of electrons recorded in a pixel.

## 3.1 Analysis

The delivered data represent the blackbody spectra ($B_\lambda(T)$: in units W/m$^2$/sr/$\mu$m), and must be converted to the incident flux ($F_\lambda$: in units of e$^-$/s/$\mu$m) `*_Flux`. These two are related by:

$$F_\lambda = B_\lambda(T)\,\Omega\,p^2\,\epsilon_\lambda \frac{Q_\lambda}{E_\lambda}, \tag{2}$$

where $\Omega$ is the solid angle projected by the component, $p$ is the size of the pixel (see Table 2, $\epsilon_\lambda$ is the dimensionless wavelength-dependent emissivity, $E_\lambda$ is the energy per photon ($= hc/\lambda$), and $Q_\lambda$ is the quantum efficiency in units of e$^-$/photon (see Figure 2). Next, we convert an astrophysical source of constant $F_\lambda$ (in units of W/m$^2$/$\mu$m) into an instrumentally-measurable intensity: $I_\lambda$ (in units of e$^-$/s/$\mu$m) via:

$$I_\lambda = F_\lambda\,A\,R_\lambda\,\frac{Q_\lambda}{E_\lambda}, \tag{3}$$

where $A$ is the collecting area of the primary mirror (see Table 2 and $R_\lambda$ is the filter response curve). As our goal is to provide a spectrum, we will ignore the filter response term and just define the inverse sensitivity ($S_\lambda$ in units of $\mu$m cm$^2$ e$^-$/erg) as the ability of the combined telescope, optics, and detector to register a photo-electron given an incident flux as:

$$S_\lambda = A\,\frac{Q_\lambda}{E_\lambda}. \tag{4}$$

As framed, the provided spectra are recorded as `*_Flux` and equivalent to the measured intensity $I_\lambda$. Combining terms, we arrive at

$$F_\lambda = B_\lambda(T)\,\Omega\,\epsilon_\lambda \frac{p^2}{A}, \tag{5}$$

as the incident flux (in erg/s/cm$^2$/$\mu$m/pix), however the final spectrum is reported as $f_\nu$ in MJy/sr.

## 3.2 Results

In Figure 3, we show the thermal spectrum derived here for each physical component in a separate panel among the $2 \times 2$ grid, with each subcomponent in a different color and the total in bold black. In the lower panel, we show the total thermal background, which is derived from the weighted sum of the totals from each of the above components. It is worth reminding the reader, this spectrum supplants the JWST model, which is *identically zero for* $\lambda < 5$ *$\mu$m*. Therefore this result represents a significant improvement to the ETC results.

Since the thermal spectrum is effectively a sum of blackbody spectra weighted by solid angle, emissivity, *etc.* (as described above), it has a significant wavelength dependence. Therefore, to characterize the relevance of this background term, we show our result (bold black line) and a notional Zodiacal spectrum (red) in the upper panel of Figure 4. We estimate the critical wavelength where the thermal contribution is larger than the Zodiacal level to be $\lambda_{\rm crit} = 1.892$ $\mu$m, and this leads us to consider the bandpass-averaged flux:

$$\left\langle F_\nu^{(c)} \right\rangle = \frac{\int F_\nu^{(c)}\,T_\nu\,{\rm d}\nu/\nu}{\int T_\nu\,{\rm d}\nu/\nu} \tag{6}$$

for each spectral component ($c$) for each bandpass. In the lower panel of Figure 4, we show the ratio of the thermal to the total as a function of the average-wavelength. From this, we find that only three bandpasses (F146, F184, and F213) have $\geq 10\%$ of their total background coming from the thermal component. These are the only bandpasses that have a significant sensitivity at $\lambda \gtrsim 1.8$ $\mu$m (note, the F146 band is extremely wide and extends to $\sim 2$ $\mu$m). Obviously, this depends on the assumed Zodiacal contribution, however this would require an extremely low Zodiacal level to change this three-bandpass finding. Moreover, these Zodiacal levels here are approximately $3-5$ times *lower* at all wavelengths than what was observed by from HST (see Figure 2 of Carleton et al. 2022).

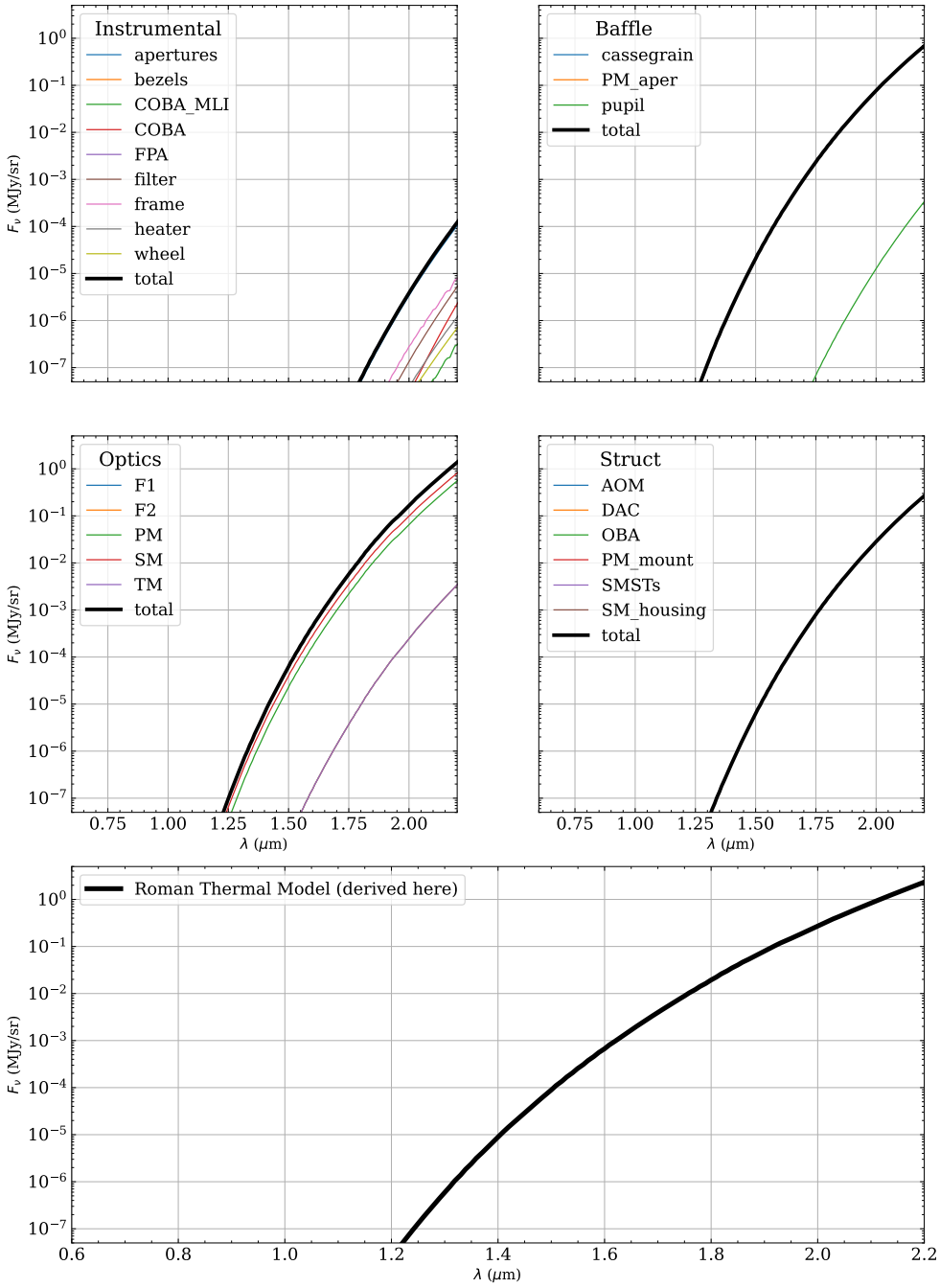


Figure 3: Thermal background spectra. In the upper grid of 2 × 2 panels, we show each component (bold black) with its individual subcomponents (colored lines). Some of the panels may be ambiguous on the non-zero contributions of different subcomponents: for the "Struct" only the SMSTs (secondary-mirror support struts) contributes any non-zero flux, and the PM_aper (primary mirror aperture) overwhelmingly dominates the "Baffle" component (it is effectively plotted under the total for this component). Finally, the bottom panel shows the total thermal spectrum, which is derived as the weighted sum of the individual total spectra from each of the upper 2 × 2 panels (see § 3.1). As noted in the text, this spectrum supplants the former model from JWST that is assumed to only be non-zero for $\lambda \geq 5$ $\mu$m, which is entirely redward of the Roman/WFI sensitivity (see Figure 2).

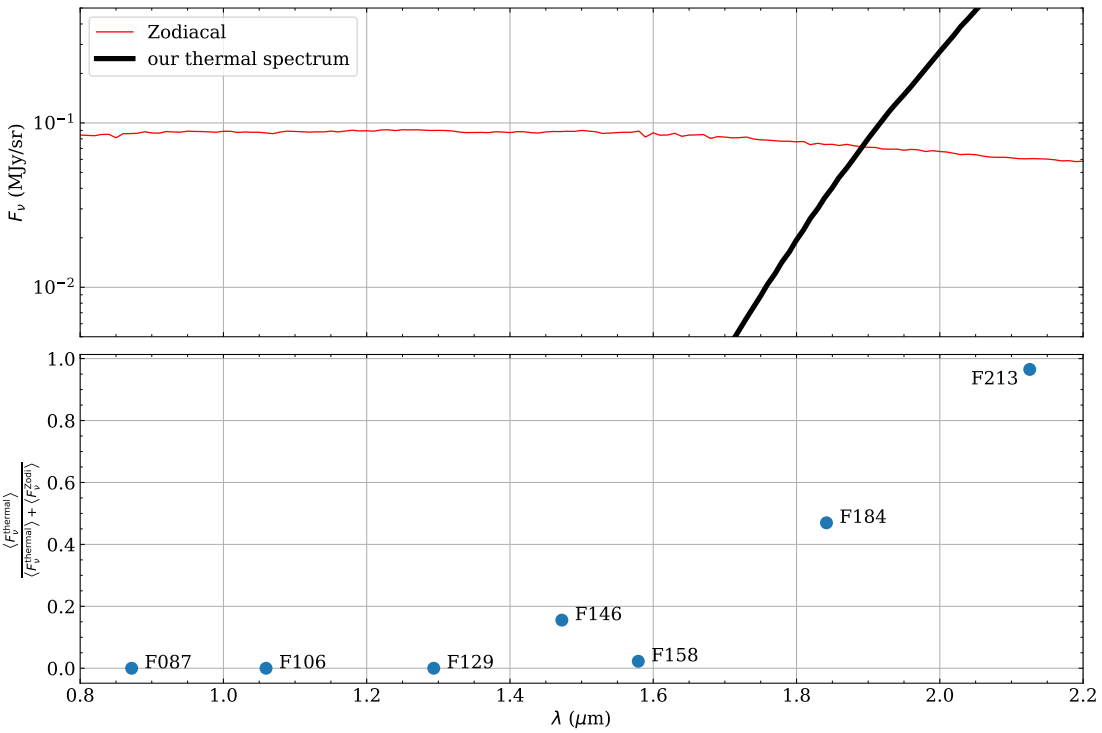


Figure 4: Comparison between thermal and Zodiacal background components. We show our thermal spectrum (bold black) and a notional Zodiacal model (thin red) to highlight the relative wavelengths where each dominates the total background. We estimate the critical wavelength where the total background is equal contribution between Zodiacal and thermal as $\lambda_{\rm crit} = 1.892$ $\mu$m. As remarked in the text, this Zodiacal spectrum is just an estimated spectrum to frame the relative strength of the thermal background. As such, one can expect observed Roman/WFI data to have the Zodiacal contribution to fluctuate and change this critical wavelength. However, we do not believe that the Zodiacal light would fluctuate so low that other bandpasses (e.g. F158) would see a significant contribution from the thermal component as this is already much lower than typical HST observations (Carleton et al. 2022). A final point, we expect the F146 band to have a modest contribution from the thermal component ($\sim$15%), despite its relatively blue central wavelength. This is a direct consequence of the very wide bandpass of the F146 band: $0.93 \lesssim \lambda \lesssim 2$ $\mu$m.

## 4 Concluding Remarks

At all stages of our analysis, we have adopted values provided by David Hughes, however as the instrument matures and in-laboratory measurements are made, some of these estimates may change and these calculations should be revisited. Similarly, on-flight measurements will be needed to validate various aspects of this model. Obviously, these re-evaluations must be propagated into the ETC and other subsystems.

*Acknowledgements* — Special thanks to David Hughes and Maxime Rizzo in understanding the physical properties and construction of the WFI, and to Adric Reidel in support of of Pandeia.

## References

Carlton, T. et al. 2022, AJ, 164, 170
Pontoppidan, K. M., et al. 2016, SPIE, 9910, 16
Spergel, D., et al. 2015, arXiv: 1503.03757